Large eddy simulations of transcritical e-fuel sprays using real-fluid multiphase flamelet-based modeling

Fathi, Mohamad; Hickel, Stefan; Roekaerts, Dirk

DOI
10.1016/j.combustflame.2025.114360

Publication date
2025

Document Version
Final published version

Published in
Combustion and Flame

Citation (APA)
Fathi, M., Hickel, S., & Roekaerts, D. (2025). Large eddy simulations of transcritical e-fuel sprays using real-fluid multiphase flamelet-based modeling. *Combustion and Flame*, *281*, Article 114360. https://doi.org/10.1016/j.combustflame.2025.114360

Combustion and Flame 281 (2025) 114360

Contents lists available at ScienceDirect

Combustion and Flame

journal homepage: www.sciencedirect.com/journal/combustion-and-flame

Large eddy simulations of transcritical e-fuel sprays using real-fluid multiphase flamelet-based modeling

Mohamad Fathi, Stefan Hickel *, Dirk Roekaerts

Delft University of Technology, Kluyverweg 1, 2629HT Delft, The Netherlands

ARTICLE INFO

Keywords:
Multiphase thermodynamics
Transcritical combustion
Tabulated chemistry
ECN spray A
Polyoxymethylene dimethyl ether

ABSTRACT

This study introduces a new numerical framework for the accurate simulation of transcritical reacting sprays using a multiphase, real-fluid, flamelet-based model. The transcritical flamelet library is combined with large-eddy simulations (LES) and rapid vapor–liquid equilibrium calculations in the context of a modern multiphase thermodynamic approach to explore vaporization dynamics, ignition characteristics, and soot formation. Current applications focus on the combustion of polyoxymethylene dimethyl ethers (OMEs), which are carbon-neutral e-fuels, in transcritical high-pressure configurations. Validation against experimental data shows a strong match in ignition delay and penetration lengths. The analysis of three OME_3– n-dodecane fuel blends reveals differences in evaporation, ignition, and soot production. Adding OME_3 to n-dodecane reduces soot production and shortens the liquid penetration length and ignition delay time. The findings highlight the importance of further investigation into the effects of transcritical states and fuel composition on combustion performance and emissions.

Novelty and significance

This work introduces a modeling technique for the use of transcritical counterflow flames in flamelet modeling, expanding the capabilities of large-eddy simulations with multiphase thermodynamics (LES-MT) to accurately modeling transcritical combustion. By incorporating real-fluid effects and two-phase interactions, the transcritical flamelet library provides a high-fidelity representation of the complex behaviors in high-pressure multiphase autoignition scenarios. This calibration-free approach can significantly improve our understanding of the transcritical combustion of emerging fuels such as OME_3 or their combination with traditional fuels such as n-dodecane.

1. Introduction

Polyoxymethylene dimethyl ethers (OMEs) are carbon-neutral e-fuels with a significant amount of oxygen in their molecular structure. The absence of C-C bonds in the chemical structure of OMEs leads to a significantly reduced soot formation and makes them practically soot-free during combustion. In addition, their high oxygen content enhances combustion efficiency and reduces carbon monoxide and particulate matter emissions [1–4]. Although previous studies have focused predominantly on OME_1 due to synthesis challenges, recent research is moving toward higher OMEs due to their favorable properties, such as boiling point, lubricity, and viscosity, which are similar to diesel [5]. This similarity allows higher OMEs to be effectively blended with conventional fuels.

Investigating the combustion properties of these green synfuels, particularly under transcritical high-pressure conditions, requires advanced simulation techniques to predict not only their emission profile but also the complex interactions in mixed fuel systems. In transcritical engines, cold liquid fuel is rapidly injected into a pressurized warm oxidizer chamber and burned through autoignition almost immediately. The term *transcritical* indicates that combustion occurs at a pressure greater than the critical pressure of the pure injectant and less than the cricondenbar of the intermediate fuel-oxidizer blend. This means that the liquid injectant can experience a hybrid combination of subcritical vaporization and supercritical direct phase change during the heating and mixing processes. The latter challenges the direct application of standard multiphase methods such as Lagrangian particle tracking and volume of fluid methods with sharp vapor–liquid interfaces, or Eulerian single-phase dense-gas approaches with diffuse vapor–liquid interfaces [6–8].

As recently shown, multiphase thermodynamics (MT) within the framework of the diffuse interface method is a highly effective and calibration-free approach to simulate transcritical fuel sprays [8,9].

---

* Corresponding author.
E-mail address: S.Hickel@tudelft.nl (S. Hickel).

https://doi.org/10.1016/j.combustflame.2025.114360
Received 12 February 2025; Received in revised form 14 July 2025; Accepted 16 July 2025

In the MT approach, the fully conservative Navier–Stokes equations (NSE) are solved to model a hypothetical multi-component fluid mixture, with thermo-transport properties derived from a suitable equation of state (EOS) in conjunction with vapor–liquid equilibrium (VLE) calculations. Despite neglecting surface tension forces, this method can accurately represent flow physics, including the subcritical region where multi-component vapor and liquid coexist and non-ideal fluid mixture behavior such as the dissolution of ambient gas in the compressed liquid.

In MT-based studies, cubic equations of state (EOSs) are widely used to model the properties of real-fluid mixtures. Most widely used are two-parameter cubic EOSs, such as SRK and PR; however, recent studies suggest that the three-parameter cubic EOS of Cismondi and Mollerup (RKPR) [10] gives superior predictions of the density close to the critical point at almost the same computational cost. For the required VLE calculations, Fathi and Hickel [11] have developed a fast phase-splitting method, with which the computational cost is almost unaffected by the number of species. This novel method is based on the molar-specific volume function allowing for rapid convergence near critical points and phase boundaries. The isoenergetic–isochoric version of their phase-splitting method can be directly applied in solvers using a conservative formulation of the compressible NSE, resulting in a considerable speedup for transcritical flows with a large number of species.

Flamelet-based combustion modeling is commonly used to simulate reacting flows with detailed chemistry. Flamelet methods are very effective at high pressures, where the flame becomes thinner and the Kolmogorov eddies cannot change the inner laminar structure of the flame [12]. Flamelet models provide an accurate representation of the actual flame through a pre-tabulating database of one-dimensional flamelets using a few controlling parameters. This can be achieved using the flamelet-generated manifold (FGM) method, which effectively incorporates transport effects into the generation of tabulated chemistry [13]. As the main combustion mode in transcritical engines is non-premixed and autoignition is inherently transient, the flamelet database is typically generated based on the results of unsteady counterflow diffusion flames (CDF) [14–16].

The ignition of CDFs is significantly influenced by the methods used to model the thermodynamic and transport properties [17]. In transcritical settings, ignoring the real-fluid effects or the two-phase region would yield an incorrect transient result. Unlike classical flamelet models based on ideal-gas assumptions, recent studies [18–21] have sought to include real-gas effects in their tabulated chemistry. The first step to consider phase separation in transcritical flamelets was taken by Traxinger et al. [22] to study transcritical combustion under rocket engine conditions. They used VLE calculations along with flamelet equations expressed in the mixture fraction space using the unitary Lewis assumption with an approximate scalar dissipation rate profile. The approach used in the present paper, as detailed in [17], constructs a flamelet-based library solving governing equations for the igniting CDF expressed in the physical space. The present model does not make a unitary Lewis assumption; instead, it utilizes detailed fugacity-based diffusion and chemistry models. It accurately captures the effects of both the two-phase region and the real-fluid properties in the flamelet database.

This paper presents a novel numerical framework to efficiently include real-fluid multiphase thermo-transport effects within an MT-based and tabulated reacting flow solver, allowing high-fidelity simulation of high-pressure transcritical fuel sprays with detailed chemistry. The transcritical flamelet library is generated using unsteady simulations of multiphase counterflow flames at transcritical pressures, including the effects of real fluids and subcritical vaporization. The fluid flow solver uses the RKPR EOS coupled with a rapid VLE solver for transcritical fluid states [11] and employs the adaptive local deconvolution method (ALDM) for large-eddy simulation (LES)-based turbulence modeling [23]. In gas turbines and diesel engines, the air–fuel mixture can easily traverse the metastable region and enter the physically forbidden (unstable) area of the two-phase dome [24]. Hence, the proposed method is first validated by comparing numerical results with the available experimental measurements for the transcritical n-dodecane Spray-A of the engine combustion network (ECN) [25,26]. To expand our understanding of the combustion characteristics of OMEs, we additionally performed Spray-A simulations using OME_3 and a mixture of OME_3 and nC_{12}, providing novel insights into the dynamics of evaporation, ignition behavior, and soot formation in different fuel configurations.

Table 1
Critical properties and acentric factors of major species.

Species	T_c [K]	p_c [bar]	Z_c	Ω
OME_3	621.5	30.20	0.247	0.507
nC_{12}	658.0	18.20	0.251	0.576
O_2	154.6	50.43	0.288	0.022
N_2	126.2	34.00	0.289	0.038

2. Transcritical sprays

The representative benchmark case of ECN Spray-A has been selected because it considers transcritical conditions typically encountered in modern internal combustion engines. The standard experimental setup involves a fuel jet at a temperature of 363 K, which is injected at a speed of approximately $600\,\mathrm{m\,s^{-1}}$ over a duration of 1.5 ms. This is achieved by a rail pressure of 1500 bar and injection through a single-hole nozzle with a nominal diameter of $D = 0.09$mm into a preheated oxidizer chamber at a temperature of 1000 K and a pressure of 60 bar. The chamber has a molar composition of $15\,\%O_2$, $6.23\,\%CO_2$, $3.62\,\%H_2O$, and $75.15\,\%N_2$. The present study focuses on three different fuel types: pure n-dodecane (nC_{12}), pure polyoxymethylene dimethyl ether 3 (OME_3), and a mixture of both with a molar composition of 50% nC_{12} and 50% OME_3.

The Spray-A operating pressure is much higher than the critical pressure of the individual fuel species, see Table 1. For all three cases, the liquid fuel experiences transcritical vaporization as it blends with the hot pressurized oxidizer. Spray-A with the diesel-like fuel nC_{12} has been extensively examined in the past. More recently, experimental data have been reported for Spray-A with OME_3 fuel. To our knowledge, no experimental or numerical studies have been conducted for the blended case.

3. Numerical models

3.1. Governing equations

Using the standard notation, the governing equations describing the conservation of mass, momentum, and total (absolute) energy for a single-fluid compressible flow can be written as

$$\partial_t \rho + \nabla \cdot (\rho \mathbf{u}) = 0, \tag{1}$$

$$\partial_t \rho \mathbf{u} + \nabla \cdot (\rho \mathbf{u}\mathbf{u} + p\mathbf{I}) = \nabla \cdot \boldsymbol{\tau}, \tag{2}$$

$$\partial_t \rho e_t + \nabla \cdot [(\rho e_t + p)\mathbf{u}] = \nabla \cdot (\mathbf{u} \cdot \boldsymbol{\tau} + \lambda \nabla T). \tag{3}$$

where ρ is the density, $\mathbf{u}$ is the velocity vector, p is the thermodynamic pressure, T is the temperature, and e_t is the total specific energy which includes the internal (absolute) energy e as well as the kinetic energy of the flow. There is no source term in the energy conservation equation, as the internal energy includes the heat of formation. λ denotes the thermal conductivity. $\boldsymbol{\tau}$ is the viscous stress tensor that is estimated using molecular viscosity μ as follows:

$$\boldsymbol{\tau} = \mu \left(\nabla \mathbf{u} + (\nabla \mathbf{u})^T \right) - 2/3\mu(\nabla \cdot \mathbf{u})\mathbf{I}. \tag{4}$$

To identify the thermodynamic state (p, T) and transport properties (λ, μ) of the working fluid, we need to know the composition in addition to the internal energy and mass density of the mixture. To avoid solving a very large number of species transport equations, the composition of the mixture is determined through a look-up table constructed based on the mixture fraction $\mathcal{Z}$ and the progress variable C as controlling parameters. The solved transport equations for the mixture fraction and the progress variable are

$$\partial_t \rho \mathcal{Z} + \nabla \cdot (\rho \mathbf{u} \mathcal{Z}) = \nabla \cdot (\lambda / c_p \nabla \mathcal{Z}) / \mathrm{Le}_{\mathcal{Z}}, \tag{5}$$

$$\partial_t \rho C + \nabla \cdot (\rho \mathbf{u} C) = \nabla \cdot (\lambda / c_p \nabla C) / \mathrm{Le}_C + \dot{\omega}_C. \tag{6}$$

The source term of the progress variable, $\dot{\omega}_C$, is also obtained from the look-up table. The Lewis numbers $\mathrm{Le}_{\mathcal{Z}}$ and Le_C of the mixture fraction and the progress variable are set to those used for the auxiliary equations in the generation of the flamelet database; see Ref. [27] for a discussion of the differential equations for $\mathcal{Z}$ and C in the presence of preferential diffusion.

In the appendix, we explain the rationale for employing the fully conservative form of the compressible Navier–Stokes equations instead of using pressure-based solvers with the low-Mach assumption.

3.2. *Multiphase thermodynamics*

The unique characteristic of the high-pressure transcritical environment is that the working fluid can cross the two-phase region and become thermodynamically unstable. Following the MT approach for modeling the real-fluid transcritical phase separation, in addition to using suitable real-gas caloric and volumetric EOSs, rapid and robust phase-splitting or flash calculations are required to account for the transcritical formation of the vapor–liquid interphase.

3.2.1. *Single-phase calculations*

A cubic EOS is often chosen as a practical balance between precision, intricacy, and computational expenses; the general form of cubic EOSs is

$$p = \mathcal{R}T / (\bar{\vartheta} - b) - a / [(\bar{\vartheta} + \delta_1 b)(\bar{\vartheta} + \delta_2 b)]. \tag{7}$$

The symbol $\mathcal{R}$ represents the universal gas constant and $\bar{\vartheta} \equiv W/\rho$ is the molar specific volume of the mixture. δ_1 and δ_2 are volume parameters. a and b are energy parameters that account for non-ideal behavior caused by attractive and repulsive forces between molecules. For real-fluid mixtures, these parameters can be determined using the van der Waals mixing rule, which can be expressed as

$$a = \sum_{i=1}^{N} \sum_{j=1}^{N} X_i X_j (1 - k_{ij}) \sqrt{a_i a_j}, \tag{8}$$

$$b = \sum_{i=1}^{N} X_i b_i, \tag{9}$$

where X_i is the mole fraction of species i. The values of a_i and b_i are determined for the pure species i, and k_{ij} represents the binary interaction coefficient between species i and j. For two-parameter cubic EOS such as SRK and PR, a_i and b_i are expressed as a general function of the acentric factor, the critical temperature, and the critical pressure of the species along with constant values for δ_1 and δ_2. The latter results in a single universal compressibility factor at the critical point and implies a systematic error in predicting the specific volume (or density) when conditions are close to the critical point. To solve this problem, Cismondi and Mollerup [10] proposed RKPR as a three-parameter EOS, in which $\delta_2 = (1 - \delta_1)/(1 + \delta_1)$ and δ_1 is a function of the compressibility factor. Using the van der Waals mixing rule, we can determine δ_1 by the following expression:

$$\delta_1 = \sum_{i=1}^{N} X_i \delta_{1,i}(\mathcal{Z}_i), \tag{10}$$

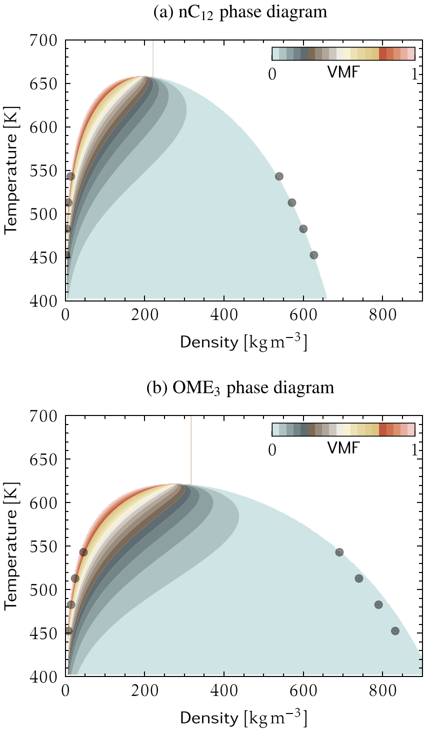

Fig. 1. Fuel phase diagrams using RKPR EOS showing vapor mole fraction (VMF) contours. The symbols show accurate reference data from Lemmon and Huber [28] for nC$_{12}$ and from Kulkarni et al. [29] for OME$_3$.

with $\mathcal{Z}_i = 1.168 Z_{c,i}$ where $Z_{c,i}$ is the critical compressibility factor of species i. We consider RKPR the most promising three-parameter cubic EOS and use it throughout this study. Phase diagrams computed using the RKPR EOS for the considered nC$_{12}$ and OME$_3$ fuels are shown in Fig. 1. The two-phase dome is highlighted using vapor mole fraction (VMF) contours, explained in the next section. The figure shows an insignificant difference between the prediction of saturated vapor and liquid density for RKPR EOS and the highly accurate EOS of Lemmon and Huber [28] and the results of the molecular simulation of Kulkarni et al. [29].

Moreover, RKPR EOS has shown reliable performance for blend system predictions. Tassin et al. [30] showed that RKPR significantly improves the phase equilibrium predictions for hydrocarbon mixtures, particularly those with highly asymmetric molecules. Kim et al. [31] further highlighted RKPR's robustness in reacting flow environments, including kerosene/LOx combustion. More recently, Fathi et al. [17] validated RKPR against experimental data for a ternary methane/n-butane/n-dodecane system, confirming its accuracy for complex multicomponent fuels.

Using Eq. (7), the thermodynamic pressure of the single-phase mixture can be calculated directly when the temperature of the mixture is known. Determining the temperature requires a caloric EOS. The caloric EOS for the single-phase real fluids can be obtained by employing the departure function formalism consistent with the utilized volumetric EOS as follows:

$$\bar{e} = \sum_{i=1}^{N} X_i \bar{h}_i^{\circ} - \mathcal{R}T + \frac{a - T \partial a / \partial T}{(\delta_2 - \delta_1) b} \ln \left(\frac{\bar{\vartheta} + \delta_1 b}{\bar{\vartheta} + \delta_2 b} \right), \tag{11}$$

with $\bar{e} \equiv e/W$ being the molar specific internal energy. The first two terms account for the absolute internal energy of the mixture at the actual temperature but at the (low) standard pressure, and the last term accounts for the internal energy change along an isothermal thermodynamic path from the standard reference pressure to the actual pressure. The molar specific enthalpy $\bar{h}_i^{\circ}$ of pure species i at the standard pressure (including the formation enthalpy) can be calculated using so-called NASA polynomials:

$$\bar{h}_i^\circ/\mathcal{R} = -a_{i,1}T^{-1} + a_{i,2}\ln T + a_{i,3}T + a_{i,4}T^2/2\ldots \\ + a_{i,5}T^3/3 + a_{i,6}T^4/4 + a_{i,7}T^5/5 + a_{i,8}, \tag{12}$$

where $a_{i,1..8}$ are polynomial coefficients of the species i, and their values for the most common species are tabulated in Ref. [32].

3.2.2. Two-phase calculations

In two-phase regions, the molar composition of the liquid and vapor phases is typically calculated using the vector of K factors, which is defined as the ratio of the mole fractions in the vapor phase (X^V) to the liquid phase (X^L), such that:

$$X_i^L = X_i/[1+\theta\left(K_i-1\right)], \tag{13}$$

$$X_i^V = X_i^L K_i, \tag{14}$$

X_i is the overall mole fraction of component i in the mixture. The vapor mole fraction θ is determined by the Rachford–Rice equation

$$\sum_{i=1}^{N} X_i(K_i-1)/[1+\theta(K_i-1)] = 0\ , \tag{15}$$

The natural logarithm of the K-factors is a complex function of the composition itself. One possible approach to estimate it initially is by using Wilson's equation, and then iteratively updating it via

$$\ln K_i = \ln\psi_i^V - \ln\psi_i^L, \tag{16}$$

where ψ is the specific volume function and can be calculated for the general cubic EOS as

$$\ln\psi_i = \ln(\bar{\vartheta}-b) - \frac{b_i}{(\bar{\vartheta}-b)} \\ + \frac{a\bar{\vartheta}b_i}{(b\mathcal{R}T)(\bar{\vartheta}+\delta_1 b)(\bar{\vartheta}+\delta_2 b)} \\ - \frac{(ab_i - 2b\varsigma_i)}{(\delta_1-\delta_2)b^2\mathcal{R}T}\ln\left(\frac{\bar{\vartheta}+\delta_1 b}{(\bar{\vartheta}+\delta_2 b)}\right), \tag{17}$$

with $\varsigma_i \equiv \sum_{j=1}^{N} X_j(1-k_{ij})\sqrt{a_i a_j}$. In addition to the thermal and mechanical phase equilibrium conditions, two more constraints are required for the unique determination of T and $\bar{\vartheta}$ of each phase. As we solve the fully conservative form of the compressible Navier–Stokes equations, that is, transport equations for energy and density, isoenergetic-isochoric phase-splitting calculations, also known as UV-flash calculations, must be performed. The two additional constraints for UV-flash calculations are

$$\bar{\vartheta} = (1-\theta)\bar{\vartheta}^L + \theta\bar{\vartheta}^V, \tag{18}$$

$$\bar{e} = (1-\theta)\bar{e}^L + \theta\bar{e}^V. \tag{19}$$

To iteratively solve the phase-splitting equations outlined above, we utilize the method of Fathi and Hickel [11], which performs rapid UV-flash calculations robustly via Newton iterations with the exact Jacobian based on an effective reduction method. We note that tabulation methods are a suitable alternative for non-reacting flows. However, when the number of species is large, both memory requirements and table query time grow unfavorably, while the cost of the Fathi–Hickel reduction method remains low and essentially independent of the number of species. For a comprehensive review and practical implementation guidelines, the readers are referred to the original article [11].

3.3. Multiphase transport properties

Thermal conductivity and dynamic viscosity of liquid and gaseous fluids at high pressures can be estimated using the correlations of Chung et al. [33]. Based on the Chung method, a transport property $\phi \in \{\lambda, \mu\}$ is a complex function of temperature, specific molar volume, molecular weight, acentric factor ω, critical molar specific volume, and critical temperature:

$$\phi = f(T, \bar{\vartheta}, W, T_c, \bar{\vartheta}_c, \Omega). \tag{20}$$

Chung et al. [33] also explain how to estimate the molecular weight, critical temperature, critical molar specific volume, and acentric factor for a mixture with a certain composition. Here, it is important to emphasize that the fundamental assumption in this context is that the mixture constitutes a solitary (stable) phase. Hence, it would be questionable to calculate the transport properties of a two-phase mixture using these correlations directly [34].

A structural model can be used to calculate the transport property of a mixture comprising two phases. As described in Ref. [34], this can be achieved by performing separate Chung calculations for the saturated liquid and vapor phases. Assuming that the vapor and liquid phases are randomly distributed within the finite-volume cells, the transport property of the mixture are computed using the effective medium theory (EMT) model [35]

$$(1-\Theta)\frac{\phi^L-\phi}{\phi^L+2\phi} + \Theta\frac{\phi^V-\phi}{\phi^V+2\phi} = 0, \tag{21}$$

with $\Theta \equiv \theta\bar{\vartheta}^V/[\theta\bar{\vartheta}^V + (1-\theta)\bar{\vartheta}^L]$ being the volume fraction of the vapor phase. The EMT model can evaluate transport properties without nonphysical oscillations or underestimations for thermal conductivity or dynamic viscosity; the interested reader is referred to Refs. [17,34] for a more detailed discussion.

3.4. Combustion modeling

Although there are many reaction mechanisms for the combustion of pure OME_3 or pure nC_{12} with air, no suitable reduced mechanism is available for their mixture. This section explains how we have developed a reduced mechanism through a decoupling methodology to cover this gap. Then, we describe our novel transcritical combustion model using MT-based real-fluid flamelet simulations in the context of the transient counterflow model (TCM).

3.4.1. Reaction mechanism

Since comprehensive reaction mechanisms of heavy fuels are usually inaccessible or too complex for direct application, the use of a suitable reduced reaction mechanism is inevitable. For our flamelet calculations in this study, we derived a reduced chemical mechanism through a decoupling methodology in which the main oxidation path of the fuels is integrated with an effective reduced C_2-C_3 mechanism and a detailed $H_2/CO/C_1$ mechanism. For the pressurized environment of internal combustion engines, Lapointe et al. [36] used this methodology and proposed an optimized reduced mechanism consisting of 65 species and 363 reactions for the oxidation of pure nC_{12}. To study blended fuels, we have added the main OME_3 oxidation pathway of Lin et al. [37] to the original Lapointe mechanism. The final hybrid mechanism used here in this study consists of 76 species and 380 reactions. The mechanism is provided as supplementary material with this article in both Cantera and Chemkin formats.

Fig. 2 illustrates the prediction of the ignition delay time (IDT) for the stoichiometric mixture of nC_{12} and OME_3 with air as the oxidizer via the proposed reaction mechanism. Here, the IDT is defined as the time at which the combustible mixture experiences a temperature rise of 400 K. The predictions based on the hybrid mechanism agree very well with those reported for experiments at a pressure of 20 bar [38,39]. For both fuels, the figure additionally shows the decrease in IDT due to the increase in pressure.

(a) nC_{12}

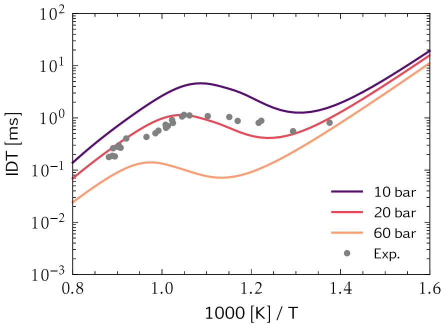

(b) OME_3

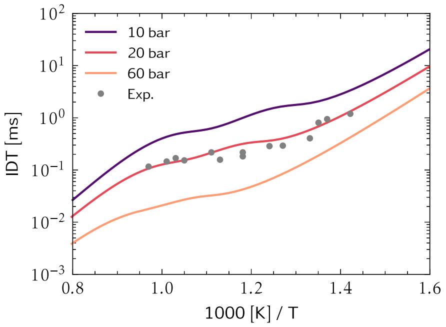

Fig. 2. Comparison of ignition delay time (IDT) of the stoichiometric air–fuel mixture calculated using the proposed hybrid mechanism (solid line) at various pressures with experimental measurements (scatter) at 20 bar [38,39].

3.4.2. *Transient counterflow model*

The main idea behind any flame-based combustion model is that turbulent eddies only distort the shape of the flame, while the inner structure of the flame remains laminar. This means that we can solve a set of laminar cases separately with detailed chemistry under conditions similar to those under the target flame and retrieve the required thermochemistry data of the main (turbulent) reacting flow using a tabulation method. To look up data, one can use a few controlling parameters representing the simulated laminar flame behavior. Typically, the control parameters that construct the manifold are a mixture fraction, indicating the state of mixing between fuel and oxidizer streams, and a progress variable that represents the degree of conversion to final products [40,41].

Counterflow flames are widely used to generate the flamelet database. For transcritical pressures, the configuration involves the injection of a liquid- or liquid-like fuel and a gaseous- or gaseous-like oxidizer in opposite directions, resulting in the formation of a reaction zone near the stagnation plane. The governing equations of unsteady transcritical counterflow flames along the axis of symmetry can be expressed as:

$$\partial_t \rho + \partial_x(\rho u) = -2\rho\mathcal{K}, \tag{22}$$

$$\rho\partial_t Y_k + \rho u \partial_x Y_k = -\partial_x \mathcal{J}_k + \dot{\omega}_k, \tag{23}$$

$$\rho\partial_t \mathcal{K} + \rho u \partial_x \mathcal{K} = \partial_x(\mu\partial_x\mathcal{K}) - \rho\mathcal{K}^2 + \rho_\infty a_\infty^2, \tag{24}$$

$$\rho c_p \partial_t T + \rho u c_p \partial_x T = \partial_x(\lambda\partial_x T) - \mathcal{J}_k \partial_x h_k - h_k \dot{\omega}_k. \tag{25}$$

where c_p is the heat capacity of the mixture. Y_k, h_k, $\mathcal{J}_k$, and $\dot{\omega}_k$ are the mass fraction, the partial enthalpy, the diffusion mass flux, and the net production rate of the species $k = 1, 2, \ldots, N$ with N being the total number of species. In the equation of the stretch rate $\mathcal{K}$, the subscript ∞ denotes the reference boundary used to evaluate the pressure curvature $\rho_\infty a_\infty^2$ where a_∞ is the applied strain rate. To solve these stiffly coupled equations, we use our in-house unsteady real-fluid flamelet solver, developed specifically for this purpose; further details are provided in the original publication [17].

The unsteady counterflow configuration required for the TCM of the target sprays is as follows. The operating pressure is 60 bar. The fuel stream at 363 K and the oxidizer stream at 1000 K are injected into a computational domain from opposite directions. This domain is initialized using the steady-state solution of the corresponding inert case. The computational domain extends from −3 mm to 3 mm and is discretized into 444 points. A uniform grid spacing of 0.002 mm is applied primarily in the center region between −0.01 mm and 0.01 mm. Outside of the central region, the grid spacing gradually increases to 0.1 mm at both ends of the domain.

Fig. 3a examines the effect of the strain rate on the IDT for three different fuels using MT-based TCM calculations. The results suggest that a strain rate of $100\,\mathrm{s}^{-1}$, which is very close to the one corresponding to the minimum IDT, is a suitable choice to accurately capture the initial stages of combustion in the target sprays. Although accounting for varying strain rates in generating the flamelet database would be more accurate, using a single representative strain rate is deemed acceptable for practical simulation purposes [42].

To accurately predict the autoignition transition, it is essential to include real-fluid thermochemical and transport effects in transcritical TCM computations. Fig. 3b shows IDT variations of n-dodecane against the applied strain rate at the oxidizer side in the TCM using different models: MT (real-gas effects with transcritical phase separation), IG (ideal-gas assumption), and IG&UL (IG with unitary Lewis number). The results strongly suggest that the unitary Lewis assumption should be avoided because of its significant impact on IDT predictions. While both MT and IG models show a similar trend, the ideal gas model clearly underestimates the ignition time.

To obtain the low-dimensional manifold, we solve Eqs. (22)–(25) along with the two transport Eqs. (5) and (6) for the mixture fraction and the reaction progress variable. In this study, Lewis numbers of the control parameters are set to $\mathrm{Le}_{\mathcal{Z}} = 1$ and $\mathrm{Le}_{\mathcal{C}} = 2$. The source term of the progress variable $\dot{\omega}_{\mathcal{C}}$ is calculated according to the oxidizer-based progress variable definition of Hadadpour et al. [15]:

$$\mathcal{C} = Y_{N_2}(Y^0_{O_2}/Y^0_{N_2}) - Y_{O_2}. \tag{26}$$

This equation subtracts the actual amount of oxygen from that in case there is no reaction. In this way, we can determine how much oxygen has been consumed locally and thus how much progress has been made in the reaction. With the mechanism used in this study, N_2 is an inert gas. Therefore, the source term of the progress variable is simply the oxygen consumption $-\dot{\omega}_{O_2}$.

Due to the strong effects of differential diffusion, the governing equation for the mixture fraction, computed by tracking the elements of the fuel composition using Bilger's definition [43], becomes very complex. To effectively resolve this issue, we solved an additional transport equation along with our flamelet governing equations for the mixture fraction [44]. The utilized mixture fraction equals the Bilger mixture fraction only when all species have unitary Lewis numbers. The amount of difference between them shows the strength of the differential diffusion effect.

Fig. 4 shows the difference between the mixture fraction based on the transport equation utilized in this study and the one computed through post-processing based on Bilger's definition for the target sprays. Due to the unsteady nature of the ignition process, the profiles are not constant, and the shaded area highlights this variation. The deviation is significant from the initial steady-state inert mixing condition to the final ignited flame, underscoring the important role of differential diffusion at transcritical pressures. It should be emphasized that the stoichiometric value of the utilized conserved scalar mixture fraction is not constant nor equal to the Bilger value.

When using unsteady flamelets to build the FGM, the selected progress variable must have a monotonic variation over time from the unburned to the burned states [45]. This results in a one-to-one mapping of each unique point in the (x, t) domain to a unique point in the 2D output codomain $(\mathcal{Z}, \mathcal{C})$, with no two different points in the domain

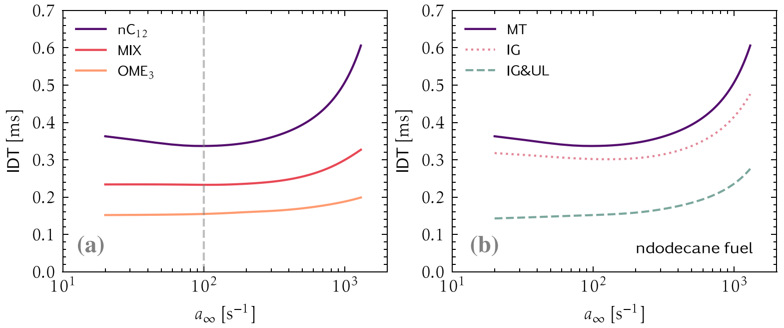

Fig. 3. Ignition delay time (IDT) as a function of applied strain rate at the oxidizer side a_∞ obtained from unsteady transcritical flamelet calculations using the proposed hybrid mechanism.

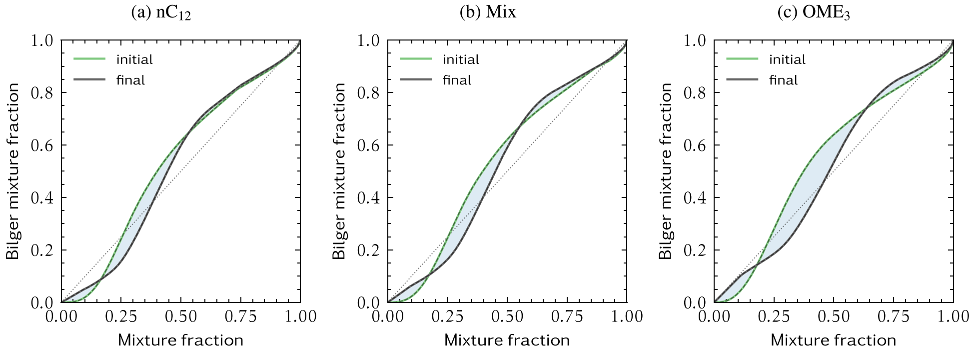
(a) nC$_{12}$ (b) Mix (c) OME$_3$

Fig. 4. Deviation of the mixture fraction from Bilger's definition for the unsteady transcritical flamelet calculation (strain rate 100 s^{-1}). The shaded region illustrates the temporal variations from the initial to the final states.

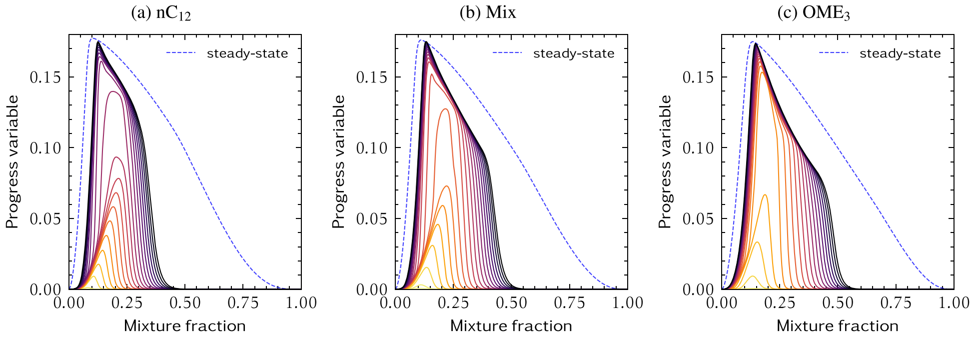
(a) nC$_{12}$ (b) Mix (c) OME$_3$

Fig. 5. Temporal evolution of the progress variable as a function of mixture fraction from the unsteady transcritical flamelet calculation (strain rate 100 s^{-1}). The blue dashed line marks the steady-state condition. Solid lines of the same color represent transient profiles at the same time.

mapping to the same point in the codomain. Fig. 5 demonstrates the monotonic characteristic for our oxidizer-based progress variable by showing the temporal profiles of C for three fuel types used to study transcritical spray-A. In all cases, there is a monotonic increase in C with time, which means that it is suitable to be used directly without further optimization [46].

Fig. 6 presents the temporal evolution of the temperature profile in the mixture fraction space for different fuels. The colored lines are plotted based on a constant time interval. The figure illustrates that the most reactive mixture fraction indicated by the peak temperature follows a similar trend for different fuels. It initially shifts toward the rich side before returning to the steady-state value. However, the rate of temperature change increases when OME$_3$ is added to nC$_{12}$ fuel. Furthermore, as indicated by the steady-state dashed lines, adding OME$_3$ causes an increase in maximum temperature. The latter indicates a higher heat release rate for OME$_3$ than for the other fuels.

Fig. 7 shows the source term of the progress variable in the mapped space of the mixture fraction and the progress variable. The source term of the progress variable, which directly influences the increase in the progress variable, plays a critical role in determining the predicted ignition delay in the LES of spray combustion. This figure displays a significant increase in the source term with higher concentrations of OME$_3$, suggesting an earlier and more rapid ignition, consistent with the previous trends observed in flamelet IDTs.

Fig. 8 presents the compressibility factor as a function of the mixture fraction, illustrating the deviation from the ideal gas law from the initial point of inert mixing to the steady-state burnt condition. As shown in the figure, the deviation from ideal gas behavior is evident from the initial to the final stage. This deviation is more pronounced for the OME$_3$ fuel than for nC$_{12}$.

Fig. 9 highlights the importance of modeling transcritical phase separation in flamelet calculations. In this figure, the two-phase region is depicted using the contours of the vapor mole fraction (VMF) for all three cases. We can see that the two-phase region in the mixture fraction — progress variable space is smaller for the OME$_3$ fuel compared to nC$_{12}$. Although in the target LES simulations, we only use the mass fractions from these flamelets and perform multiphase thermodynamics calculations based on the density and internal energy

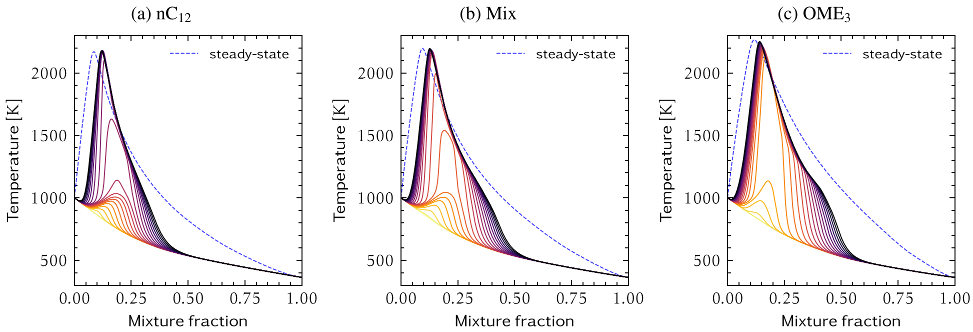

Fig. 6. Temporal evolution of the temperature as a function of mixture fraction from the unsteady transcritical flamelet calculation (strain rate $100\,\mathrm{s}^{-1}$). The blue dashed line marks the steady-state condition. Solid lines of the same color represent transient profiles at the same time.

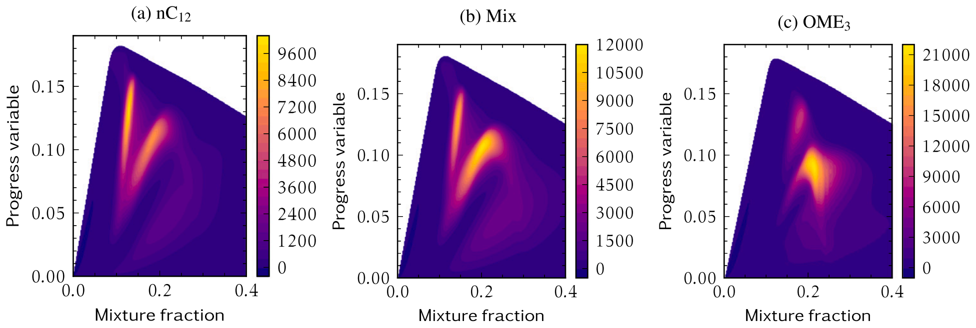

Fig. 7. Progress variable source term $\dot{\omega}_c$ as a function of the mixture fraction and progress variable generated based on the transient counterflow model.

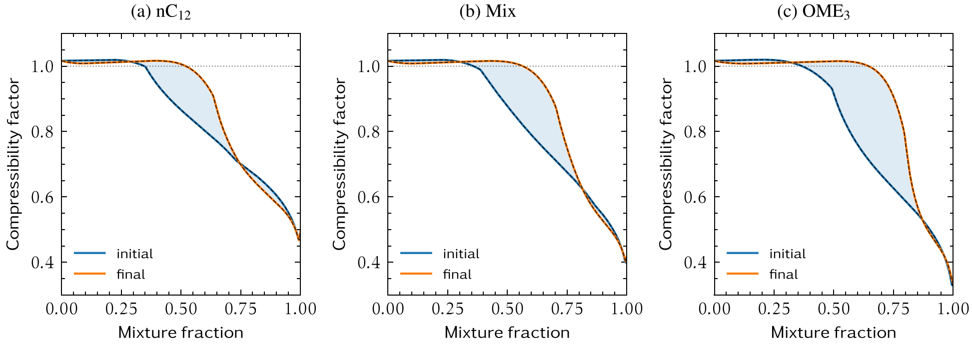

Fig. 8. Compressibility factor as a function of the mixture fraction computed for the unsteady transcritical flamelet calculation (strain rate $100\,\mathrm{s}^{-1}$). The shaded region illustrates the temporal variations from the initial to the final states.

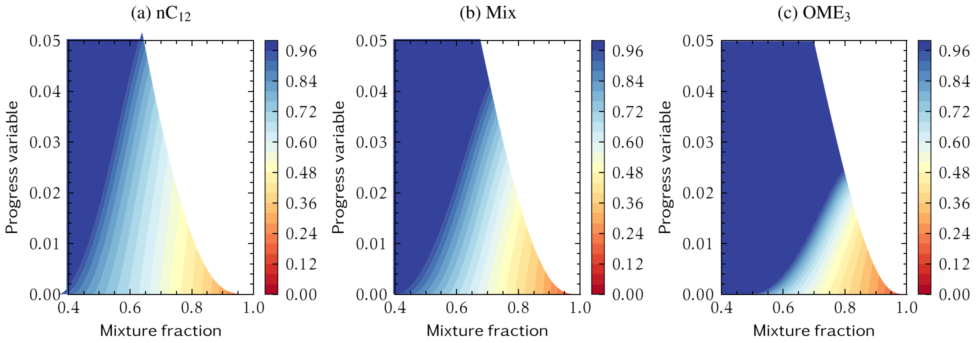

Fig. 9. Vapor mole fraction (VMF) θ as a function of the mixture fraction and progress variable generated based on the transient counterflow model.

of the flow to determine whether the mixture is in a two-phase or single-phase state, the tabulated VLE information from flamelets can significantly accelerate the iterative thermodynamic calculations by providing a suitable initial guess.

3.5. Flow-turbulence interactions

Large eddy simulation (LES) offers a detailed representation of the large scales of fluid motion that dominate the mechanical energy of turbulent flows. These large scales are governed by a coarse-grained or low-pass-filtered form of the Navier–Stokes equations in which the effects of the interactions between represented and unrepresented scales are included through appropriate subgrid-scale (SGS) modeling. In a finite-volume framework, the need for SGS modeling directly originates in the residual of the non-linear fluxes, that is, in the limited ability to represent the exact flux across cell faces with discrete reconstruction operators. Thus, turbulence modeling and numerical discretization are intrinsically linked. We use the LES method of Hickel et al. [23], which is based on a nonlinear, solution-adaptive flux reconstruction method and spectral turbulence theory. The method is well suited for applications across all Mach numbers and has been extensively verified and validated for reacting and non-reacting transcritical fuel injectors [8,47]. For simplicity of the computations and following common practice, we neglect SGS terms that arise from low-pass filtering the non-linear equations used to evaluate the properties of real fluids [9]. Furthermore, the interactions between SGS turbulence and combustion can be neglected in the context of ALDM with sufficiently fine spatial and temporal resolution, as shown in Ref. [8]. Since the same grid resolutions and turbulence modeling are used in this study, we opted not to include the variances of the progress variable and the mixture fraction, see Egüz et al. [48] for a detailed analysis of the effects of the turbulence–combustion interaction in the diesel spray context.

4. Simulation setup

4.1. Multi-block structured grid

All simulations have been carried out using a multi-block structured grid generated in a rectangular cubic domain with a size of $84 \times 42 \times 42\,\mathrm{mm}$. We utilize the INCA flow solver (https://inca.cfd) with static zonal mesh refinement within a user-defined region of interest [8]. This region is defined as a 10° cone encompassing the injected jet. The level of refinement within this cone is strategically determined by the distance from the injector nozzle, with specific resolution steps at axial locations 60, 37, 23, 14, 9 and 5.5 mm from the injector nozzle. The resulting multi-block structured grid comprises 2864 blocks and 12.7×10^6 cells distributed in seven resolution levels (L1 to L7). Approximately 40 % of the cells are concentrated on the finest level L7, with $\Delta y_{\mathrm{min}} = \Delta z_{\mathrm{min}} \simeq 10.25\,\mu\mathrm{m}$ and $\Delta x_{\mathrm{min}} = 2\Delta y_{\mathrm{min}}$ near the nozzle region.

4.2. Boundary conditions

A transient inflow velocity boundary condition is implemented in the exit plane of the fuel injector. For all types of fuel cases, the inflow velocity is calculated to provide the same amount of momentum as in the standard case of ECN Spray-A. Similar to our previous study [17], we first calculated the mass flow rate using the clean mobility and thermofluids (CMT) virtual injection rate generator (https://www.cmt.upv.es), with input parameters that match the experimental conditions and fuel densities calculated using the RKPR EOS at the injection pressure and temperature of bar60 and 363 K. Then, we computed the required inflow velocity using the fuel density. Fig. 10 illustrates the transient injection velocity generated for all fuel cases. The transient velocity profile is used in a subsonic inlet boundary condition without adding any artificial turbulent fluctuations. Fluctuations induced by shear and hydrodynamic pressure are expected to be strong enough to create turbulence almost instantaneously.

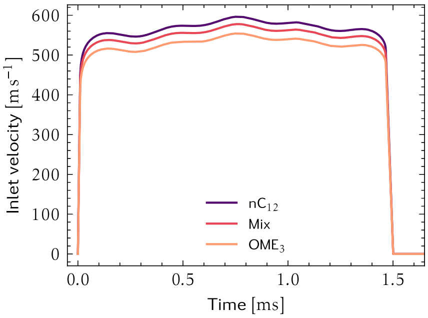

Fig. 10. Transient injection velocity profile for Spray-A test cases using RKPR EOS.

Subsonic outflow boundary conditions are imposed on the opposite end of the domain, where a consistent static pressure of 60 bar is specified as the Dirichlet condition, and the remaining flow variables are extrapolated from the internal domain. Adiabatic no-slip conditions are enforced on all other boundaries of the computation domain.

4.3. Tabulated chemistry

In the present combustion model, the mass fractions of the species are determined by the mixture fraction and the progress variable. For this purpose, a two-dimensional manifold is created for each fuel, using 256 x 1024 points to represent the table space based on the mixture fraction and the dimensionless progress variable. The dimensionless progress variable is computed via $C_s \equiv C/C_b(\mathcal{Z})$. The subscript b denotes the values obtained from the final burnt state. The blue dotted line in Fig. 5, shows the mixture fraction functionality of $C_b(\mathcal{Z})$.

4.4. Flow solver

All numerical models are implemented in our INCA flow solver (https://inca.cfd) with the same discretization techniques used in our previous work [8]. The governing equations are spatially discretized using a conservative finite-volume scheme. A second-order central difference method is utilized for viscous terms and ALDM for inviscid fluxes [23]. The van Albada limiter prevents spurious oscillations at sharp density gradients for mass- and energy-flux reconstruction.

A second-order Strang splitting method separates the chemical reactions from the advection and diffusion processes. This separation is required because the VLE calculations are only valid for non-reacting mixtures. The splitting approach comprises three main stages: Initially, the solution is advanced by incorporating solely the source term of the progress variable in a half-time step. For this step, we used the explicit sixth-order Runge–Kutta technique developed by Verner [49]. Subsequently, the updated solution is set as the initial state for the progress variable, which is used to determine the new composition from the lookup table and update the necessary thermo-transport properties for a complete advection and diffusion time step. For the non-reacting step, we utilized the explicit third-order strong stability-preserving Runge–Kutta method proposed by Gottlieb and Shu [50]. Finally, the solution is further advanced with the second half of the time step similar to the initial one. The time-step size is dynamically adjusted by the Courant–Friedrichs–Lewy stability criterion with a unitary CFL number.

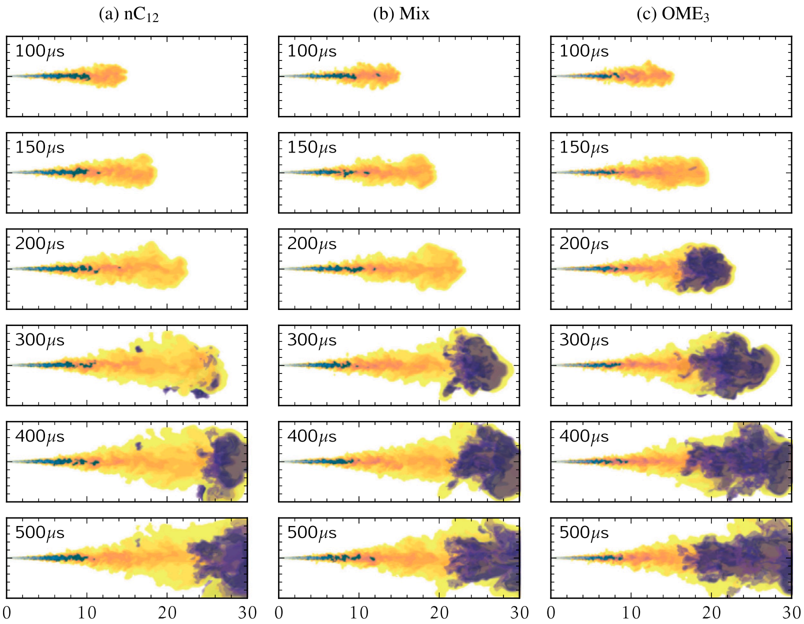

Fig. 11. Time sequence snapshots of reacting spray-A with different fuels. The light background contours display the mixture fraction, overlaid with the green contours of liquid volume fraction in the two-phase region. The deep purple area shows the temperature isosurface at 1800 K.

5. Results

This section addresses two primary objectives. First, it aims to validate the proposed multiphase flamelet-based solver for accurately modeling transcritical combustion processes, emphasizing its capacity to capture key spray characteristics, including vaporization behavior and ignition dynamics. Second, we present a comprehensive comparison of the spray-A performance for pure nC_{12}, pure OME_3, and their mixture under identical transcritical conditions. The analysis includes a detailed examination of transcritical vaporization phenomena, highlighting the differential evaporation rates of fuel components and the interaction between the liquid fuel and the surrounding environment. We also investigate ignition characteristics, focusing on ignition times and penetration lengths, as well as the evolution of various combustion zones, including two-phase, cool-flame, and high-temperature regions. Finally, the study evaluates the formation of soot using acetylene (C_2H_2) as a key precursor, offering insight into the impact of fuel composition on emissions.

5.1. Overview and temporal evolution

The temporal evolution of the reacting Spray-A with three different fuels is illustrated in Fig. 11, displaying instantaneous snapshots of the solution. Here, the two-phase region is represented by the liquid volume fraction (LVF) contours, shown in green, which also indicate the predicted distribution of the liquid injectant in the transcritical combustion chamber. With regard to ignition delay time (IDT), a good agreement is observed between the available experimental data from CMT [25] and the results of LES in the current work, using the reduced hybrid reaction mechanism within the flamelet modeling framework based on MT. These ignition times are summarized in Table 2 and are defined based on a temperature increase of 400 K above the initial ambient temperature.

The ignition process across all fuel cases shows similar behavior, where around the ignition time, low-temperature reactions are activated in a substantial portion of the vaporized fuel. The iso-temperature surface at 1800 K is used to highlight the most reactive regions (Fig. 11, deep purple). The transition to high-temperature ignition is characterized by a rapid, volumetric expansion, with an abrupt radial spread of the reacting jet observed in proximity to the flame front.

Table 2
Ignition delay time predicted by the available experiments [25] and current work simulations.

	nC_{12}	Mix	OME_3
IDT (LES)	242 μs	214 μs	149 μs
IDT (EXP)	294 μs	–	194 μs

Table 3
Liquid penetration length predicted by the available experiment [26] and current work simulations. The unit of numbers is mm.

	nC_{12}	Mix	OME_3
LPL (LES)	9.8	8.8	7.9
LPL (EXP)	9.4	–	–

Fig. 12 presents the temporal evolution of the liquid penetration length (LPL) and the vapor penetration length (VPL) for the present simulations alongside the experimental measurements [25]. For our LES, LPL and VPL are defined as the maximum axial positions where the liquid volume fraction (LVF) is 5% and the mixture fraction is 1%, respectively. The results demonstrate excellent agreement between the LES and the experimental data for both LPL and VPL. It should be noted that experimental data for the mixed fuel case are not available and for pure OME_3, data from OMEx, a mixture of OME_3 and OME_4, were used as reference. The LPL values, which are listed in Table 3, show close agreement with Sandia experimental data reported for the nC_{12} case. In line with the comparative study of Xuan et al. [51], our results demonstrate that the liquid penetration length is indeed shorter for OME_3 than for nC_{12}. This supports the conclusion that OME_3's lower boiling point is more influential on the vaporization length than its higher latent heat of vaporization or density.

5.2. Ignition zones

Fig. 13 illustrates the three main zones in transcritical reacting sprays: (1) the two-phase region, influenced by fuel properties and injection conditions, (2) the cool flame region marked by CH_2O formation, indicating low-temperature reactions and first-stage ignition,

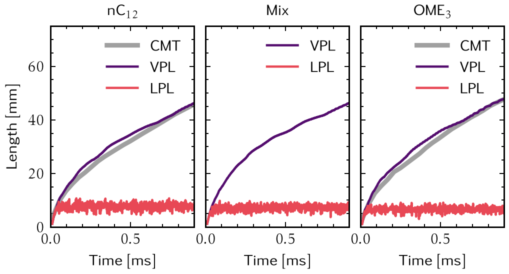

Fig. 12. Comparison between CMT experiments [25] and current LES for the vapor penetration length (VPL) and liquid penetration length (LPL) for all fuels. The uncertainty of the measurements is expressed by the line thickness.

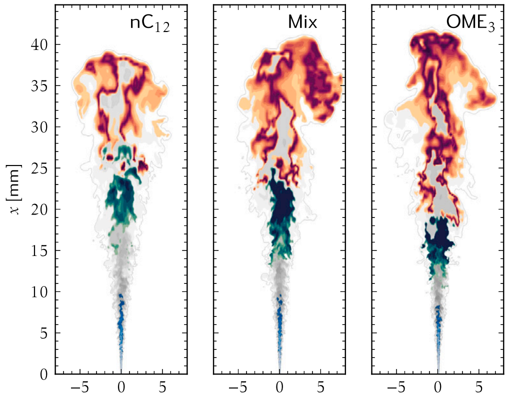

Fig. 13. Comparison of two-phase region (in blue), hot and cold flame regions marked by OH (in red) and CH$_2$O (in green) distribution for different fuels at 670 μs after the fuel injection.

Table 4
Lift-off length of hot and cold spray flames. Numbers are in mm.

	nC$_{12}$	Mix	OME$_3$
LOL (Hot Flame)	24.6	22.3	16.1
LOL (Cold Flame)	15.2	13.3	10.4

and (3) the high-temperature reaction zone, highlighted by OH radicals, representing second-stage ignition and complete combustion.

In general, the addition of OME$_3$ to the n-dodecane fuel results in several significant changes in the three characteristic zones. The length of the two-phase region is reduced. The lift-off length of the cool flame also decreases, which indicates a shorter distance from the nozzle where ignition initiates. Moreover, the overall length of the cool flame region also decreases, leading to the formation of the hot flame in closer proximity to the nozzle, with an extended flame length; see Table 4. Another notable effect of adding OME$_3$ is the disappearance of the overlap between the cool flame and hot flame regions, which can be attributed to differences in their stoichiometric and most ignitable mixture fraction. These findings align with experimental results reported by Pastor et al. [25] regarding the lift-off length (LOL) of Spray-A under similar conditions. They observed a 20 % reduction in LOL for oxygenated fuel OMEx compared to n-dodecane. The measured LOL values were 13.7 mm for OMEx and 16.6 mm for n-dodecane, respectively.

The auto-ignition process is depicted in Fig. 14 through global scatter plots of temperature within mixture fraction space at various time instants (0.5, 1.0, 1.1, and 1.5 times the ignition time). The figure illustrates that the first and second stages of the ignition for pure OME$_3$ fuel start at regions with lower oxygen concentration (i.e., higher mixture fraction) compared to pure n-dodecane. In the case of mixed fuel, the behavior falls between the two pure fuel cases, reflecting characteristics of both fuels during the ignition process.

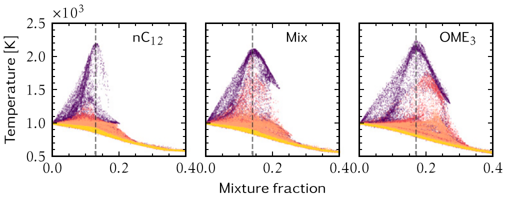

Fig. 14. Mixture fraction-temperature map for different fuel sprays at 0.5 (yellow), 1.0 (orange), 1.1 (red), and 1.5 (purple) times of the ignition time.

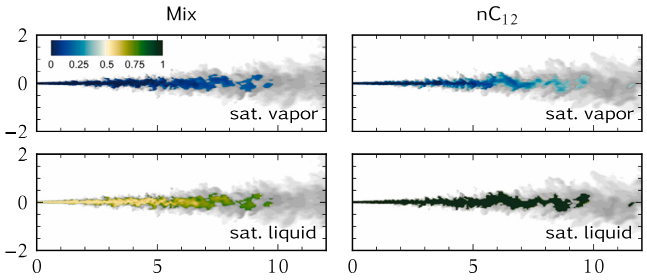

Fig. 15. Comparison of transcritical evaporation of n-dodecane for pure nC$_{12}$ and mixed fuel (nC$_{12}$/OME$_3$) cases. Contours show mass fraction of n-dodecane in the two-phase region for the saturated vapor and the saturated liquid.

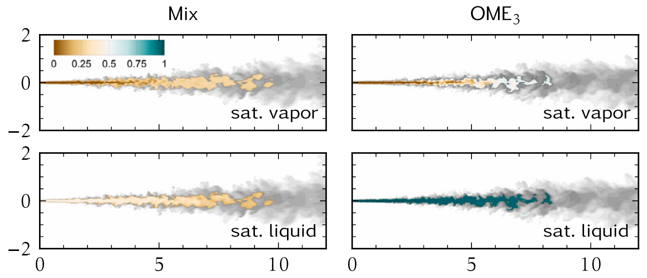

Fig. 16. Comparison of transcritical evaporation of OME$_3$ for pure OME$_3$ and mixed fuel (nC$_{12}$/OME$_3$) cases. Contours show mass fraction of OME$_3$ in the two-phase region for the saturated vapor and the saturated liquid.

5.3. Transcritical vaporization

Fig. 15 compares the transcritical evaporation of n-dodecane for pure n-dodecane and mixed fuel scenarios. In both cases, the saturated vapor of n-dodecane becomes progressively richer as it travels through the combustion chamber, driven by the increased evaporation of the liquid phase. For pure n-dodecane, the saturated liquid jet undergoes a negligible dissolution of the surrounding ambient gases (less than 3%), resulting in a relatively constant composition from the inlet to the tip of the liquid jet. In contrast, for the mixed fuel scenario, the n-dodecane mass fraction within the liquid jet increases from the initial 50% at the inlet to about 75% at the jet tip. This behavior is directly attributed to the differential evaporation rates of OME$_3$ and nC$_{12}$ species. OME$_3$ has a higher volatility than nC$_{12}$, resulting in the enrichment of the saturated liquid phase in n-dodecane as the jet advances.

Fig. 16 illustrates the transcritical evaporation of OME$_3$ for two scenarios: a mixed fuel (n-dodecane/OME$_3$) and pure OME$_3$. In both cases, the saturated vapor becomes progressively enriched in OME$_3$ as it penetrates further into the chamber due to the heat absorption from the surroundings that drives the phase change from liquid to vapor. For pure OME$_3$, the liquid jet composition changes insignificantly from the nozzle to the jet tip, indicating that a negligible amount of ambient

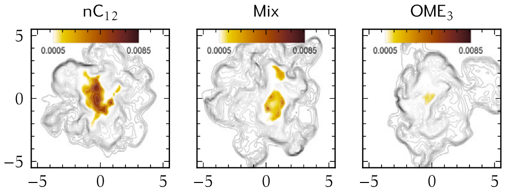

Fig. 17. Acetylene mass fraction contours on a plane normal to the axial direction at $x = 30$mm and 670 μs after the start of the injection. The background shows temperature contour lines.

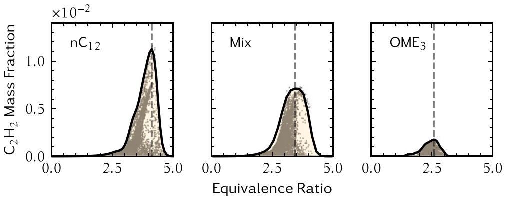

Fig. 18. Equivalence ratio-acetylene map for sprays with different fuels. The scatter points show data at 670 μs after the start of the injection. The solid lines show a Gaussian curve fit through the upper points. The dashed lines show the location of the peak of the fitted curves.

gas (less than 5%) dissolves into the liquid. However, in the mixed fuel case, the mass fraction of OME$_3$ in the liquid phase decreases from the initial 50% at the nozzle to about 25% at the jet tip, suggesting that OME$_3$ evaporates more rapidly compared to n-dodecane.

5.4. Soot formation

The present simulations do not include detailed models for the formation of soot particles; however, they represent key precursors in the formation of soot that directly contribute to the growth of soot particles during combustion. Fig. 17 presents the contours of C_2H_2 (acetylene) for the developed flame at a distance larger than the lift-off length (LOL) for all fuel cases. Due to the absence of C–C bonds, OME$_3$ burns almost soot-free, while the nC$_{12}$ and Mix fuel cases show considerable concentrations of C_2H_2 within the core flame region, indicating a higher propensity to soot formation. As anticipated, the addition of OME$_3$ to nC$_{12}$ can reduce the C_2H_2 levels; the maximum acetylene concentration observed for the mixed fuel is less than half of that for pure dodecane in this snapshot section.

Fig. 18 illustrates the global C_2H_2 mass fraction versus the local equivalence ratio for the three sprays. The LES results show that acetylene forms in equivalence ratios between 2.5 and 5.0 for the n-dodecane fuel. Pastor et al. [25] reported an upper limit of 5.5 in a similar context. For mixed fuel, acetylene forms between 2.0 and 4.5 and for OME$_3$, between 2.0 and 3.0. Peak values are marked with dashed lines in Fig. 18. The lower ϕ for peak values for the Mix and OME$_3$ cases are mainly related to their lower stoichiometric air–fuel ratios, which are 15.59 and 8.59, respectively, compared to 21.18 for nC$_{12}$. The figure confirms that the OME$_3$ spray flame can be expected to be nearly soot-free, but the two other flames create a noticeable amount of C_2H_2. For Spray-A with nC$_{12}$ fuel, the amount of acetylene produced, $\int \rho Y_{C_2H_2} \mathrm{d}V$, is approximately 1.76×10^{-9} kg at 1000 μs after the start of the injection. This amount decreases by about 25 % for the mixed fuel, reaching approximately 1.29×10^{-9} kg at the same time. This modest reduction can be explained by considering the effect of the faster evaporation rate of OME$_3$, resulting in a rapid depletion of OME$_3$ in the fuel mixture and an initial enrichment of the remaining nC$_{12}$. This procedure shifts the combustion of n-dodecane to occur in a more fuel-rich environment, especially in regions with a higher mixture fraction, thereby lowering the local oxygen concentration available during the ignition phase. Lower oxygen availability at the start of combustion leads to increased production of C_2H_2. Lastly, we note that the same bulk strain is used in the generation of all chemistry tables. Consequently, the observed reduction is not related to flame straining, as presented in [42]; rather, it is directly a result of changes in fuel composition.

6. Conclusions

We have presented a new method for high-fidelity simulations of transcritical combustion using a real-fluid multiphase thermo-transport solver based on the LES-MT framework with a transcritical flamelet library. This model effectively combines detailed chemical kinetics with multiphase interactions in complex fuel sprays. Validation against experimental data for Spray-A with n-dodecane fueling confirms the accuracy of the LES-MT approach in predicting ignition delay time, vapor penetration length, and liquid penetration length under transcritical conditions.

LES-MT results indicate distinct differences in the behaviors of transcritical evaporation, ignition, and soot formation between the injection of pure n-dodecane, pure OME$_3$, and a nC$_{12}$– OME$_3$ fuel mixture. Adding OME$_3$ to nC$_{12}$ shortens the two-phase region and reduces the lift-off length of the cool flame, resulting in earlier ignition. Although OME$_3$ shows an advantage in being nearly soot-free, the mixed fuel case shows a surprisingly modest reduction of soot formation due to fuel-rich conditions and reduced oxygen availability, driven by OME$_3$'s faster evaporation. These findings, based on the proposed reduced hybrid reaction mechanism, underscore the need for further studies to fully understand the complex interactions in mixed fuels under varying conditions.

CRediT authorship contribution statement

Mohamad Fathi: Writing – original draft, Visualization, Validation, Software, Methodology, Investigation, Formal analysis, Data curation, Conceptualization. **Stefan Hickel:** Writing – review & editing, Supervision, Software, Resources, Project administration, Methodology, Funding acquisition, Conceptualization. **Dirk Roekaerts:** Writing – review & editing, Supervision, Methodology, Conceptualization.

Declaration of competing interest

The authors declare that they have no known competing financial interests or personal relationships that could have appeared to influence the work reported in this paper.

Acknowledgments

This work was partially funded by The Netherlands Organization for Scientific Research (NWO) under Contract No. 680.91.082. We acknowledge the Delft High Performance Computing Centre (DHPC) for providing computational resources for the presented simulations.

Appendix A

Although pressure-based solvers that operate under low-Mach assumptions can be accurate and efficient in many cases, like those used by Traxinger et al. [22], they are not ideal for test cases such as the ECN Spray-A configuration. In the Spray-A setup, the speed of sound in the liquid phase is approximately 900 m s^{-1}, but it can decrease to values lower than 300 m s^{-1} in the vaporized regions. With injection velocities close to 600 m s^{-1}, local Mach numbers often exceed unity, as illustrated in Fig. 19. Solving the fully conservative compressible Navier–Stokes equations is, therefore, essential to accurately capture dynamic pressure changes, shock waves, and phase transitions [9]. Manifold retrieval techniques, which separate pressure from thermodynamic states, fall short in such dynamic settings. In contrast, the on-the-fly UV-flash method, updating internal energy and volume in real time, maintains a

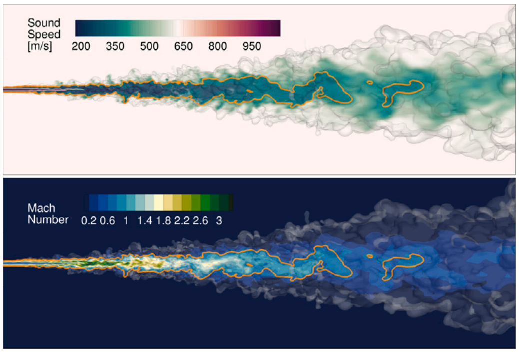

Fig. 19. Mid-plane contours of speed of sound and Mach number along with a 3D rendering of mixture fraction iso-surface of 0.001. The orange line shows the edge of the vaporizing region.

tight coupling of thermodynamic and pressure fields in all flow regions. For this reason, we use on-the-fly UV flash calculations instead of manifold retrieval in this paper, similar as the compressible flamelet approach proposed by Saghafian et al. [52].

The UV-flash method [11] is optimized for computational efficiency and remains efficient regardless of the number of chemical species monitored. This makes it suitable for LES of multi-component fuels in high-pressure, turbulent spray environments. However, the intricate nature of such modeling can significantly increase local computational expenses, often causing an uneven distribution of workload with a traditional domain decomposition. Thus, employing dynamic load balancing strategies [53] is crucial to maintain parallel scalability of simulations that feature detailed spray flame modeling.

Appendix B. Supplementary data

The hybrid reaction mechanism with 76 species and 380 reactions is provided in Chemkin and Cantera format.

Supplementary material related to this article can be found online at https://doi.org/10.1016/j.combustflame.2025.114360.

References

[1] J. Liu, H. Wang, Y. Li, Z. Zheng, Z. Xue, H. Shang, M. Yao, Effects of diesel/PODE (polyoxymethylene dimethyl ethers) blends on combustion and emission characteristics in a heavy duty diesel engine, Fuel 177 (2016) 206–216.
[2] R. Novella, G. Bracho, J. Gomez-Soriano, C.S. Fernandes, T. Lucchini, Combustion system optimization for the integration of e-fuels (oxymethylene ether) in compression ignition engines, Fuel 305 (2021) 121580.
[3] F. Ferraro, C. Russo, R. Schmitz, C. Hasse, M. Sirignano, Experimental and numerical study on the effect of oxymethylene ether-3 (OME3) on soot particle formation, Fuel 286 (2021) 119353.
[4] R. Schmitz, C. Russo, F. Ferraro, B. Apicella, C. Hasse, M. Sirignano, Effect of oxymethylene ether-2-3-4 (OME2-4) on soot particle formation and chemical features, Fuel 324 (2022) 124617.
[5] H. Pitsch, D. Goeb, L. Cai, W. Willems, Potential of oxymethylene ethers as renewable diesel substitute, Prog. Energ. Combust. 104 (2024) 101173.
[6] L. Jofre, J. Urzay, Transcritical diffuse-interface hydrodynamics of propellants in high-pressure combustors of chemical propulsion systems, Prog. Energ. Combust. 82 (2021) 100877.
[7] C. Crua, J. Manin, L.M. Pickett, On the transcritical mixing of fuels at diesel engine conditions, Fuel 208 (2017) 535–548.
[8] M. Fathi, S. Hickel, D. Roekaerts, Large eddy simulations of reacting and non-reacting transcritical fuel sprays using multiphase thermodynamics, Phys. Fluids 34 (2022).
[9] J. Matheis, S. Hickel, Multi-component vapor-liquid equilibrium model for LES of high-pressure fuel injection and application to ECN Spray A, Int. J. Multiphas Flow 99 (2018) 294–311.
[10] M. Cismondi, J. Mollerup, Development and application of a three-parameter RK–PR equation of state, Fluid Phase Equilib. 232 (2005) 74–89.
[11] M. Fathi, S. Hickel, Rapid multi-component phase-split calculations using volume functions and reduction methods, AIChE J. 67 (2021) e17174.
[12] F. Bracco, Structure of flames in premixed-charge IC engines, Combust. Sci. Technol. 58 (1988) 209–230.
[13] J. van Oijen, A. Donini, R. Bastiaans, J. ten Thije Boonkkamp, L. de Goey, State-of-the-art in premixed combustion modeling using flamelet generated manifolds, Prog. Energ. Combust. 57 (2016) 30–74.
[14] A. Wehrfritz, O. Kaario, V. Vuorinen, B. Somers, Large Eddy Simulation of n-dodecane spray flames using Flamelet Generated Manifolds, Combust. Flame 167 (2016) 113–131.
[15] A. Hadadpour, S. Xu, Y. Zhang, X.-S. Bai, M. Jangi, An extended FGM model with transported PDF for LES of spray combustion, Proc. Combust. Inst. 39 (2023) 4889–4898.
[16] C. Sula, H. Grosshans, M.V. Papalexandris, Numerical study of spray combustion of a biodiesel surrogate fuel using the LES-FGM approach, Combust. Flame 249 (2023) 112611.
[17] M. Fathi, D. Roekaerts, S. Hickel, Numerical simulation of transcritical multiphase combustion using real-fluid thermochemical and transport properties, Combust. Flame 275 (2025) 114055.
[18] J.-P. Hickey, M. Ihme, Large eddy simulation of supercritical mixing and combustion for rocket applications, in: 52nd Aero Sci Meeting, 2014, p. 0138.
[19] Z. Gao, H. Wang, C. Song, K. Luo, J. Fan, Large-eddy simulation of hydrothermal flames using extended flamelet/progress variable approach, J. Supercrit Fluid 163 (2020) 104843.
[20] H. Müller, M. Pfitzner, A flamelet model for transcritical LOx/GCH4 flames, J. Phys. Conf. Ser. 821 (2017-03) 012010.
[21] J. Zips, H. Müller, M. Pfitzner, Efficient thermo-chemistry tabulation for non-premixed combustion at high-pressure conditions, Flow Turbul. Combust. 101 (2018) 821–850.
[22] C. Traxinger, J. Zips, M. Pfitzner, Single-phase instability in non-premixed flames under liquid rocket engine relevant conditions, J. Propul. Power 35 (4) (2019) 675–689.
[23] S. Hickel, C. Egerer, J. Larsson, Subgrid-scale modeling for implicit large eddy simulation of compressible flows and shock-turbulence interaction, Phys. Fluids 26 (2014) 106101.
[24] P.C. Ma, H. Wu, D.T. Banuti, M. Ihme, On the numerical behavior of diffuse-interface methods for transcritical real-fluids simulations, Int. J. Multiphas Flow 113 (2019) 231–249.
[25] J.V. Pastor, J.M. García-Oliver, C. Micó, A.A. García-Carrero, An experimental study with renewable fuels using ECN spray a and d nozzles, Int. J. Eng. Res. 23 (2022) 1748–1759.
[26] J. Abraham, L.M. Pickett, Computed and measured fuel vapor distribution in a diesel spray, At. Spray 20 (2010).
[27] N. Mukundakumar, D. Efimov, N. Beishuizen, J. van Oijen, A new preferential diffusion model applied to FGM simulations of hydrogen flames, Combust Theory Model. 25 (2021) 1245–1267.
[28] E.W. Lemmon, M.L. Huber, Thermodynamic properties of n-dodecane, Energy Fuels 18 (2004) 960–967.
[29] A. Kulkarni, E.J. García, A. Damone, M. Schappals, S. Stephan, M. Kohns, H. Hasse, A force field for poly (oxymethylene) dimethyl ethers (OMEn), J. Chem. Theory Comput. 16 (2020) 2517–2528.
[30] N. Tassin, V. Mascietti, M. Cismondi, Phase behavior of multicomponent alkane mixtures and evaluation of predictive capacity for the PR and RKPR EoS's, Fluid Phase Equilib. 480 (2019) 53–65.
[31] S. Kim, H. Choi, Y. Kim, Thermodynamic modeling based on a generalized cubic equation of state for kerosene/LOx rocket combustion, Combust. Flame 159 (3) (2012) 1351–1365.
[32] A. Burcat, B. Ruscic, Third millenium ideal gas and condensed phase thermochemical database for combustion (with upyear from active thermochemical tables), Tech. Rep., Argonne National Lab.(ANL), Argonne, IL (United States), 2005.
[33] T.H. Chung, M. Ajlan, L.L. Lee, K.E. Starling, Generalized multiparameter correlation for nonpolar and polar fluid transport properties, Ind. Eng. Chem. Res. 27 (1988) 671–679.
[34] M. Fathi, S. Hickel, D. Roekaerts, Numerical simulations of real-fluid reacting sprays at transcritical pressures using multiphase thermodynamics, in: Int Sem on NICFD Prop Power, Springer, 2022, pp. 169–177.
[35] J. Wang, J.K. Carson, M.F. North, D.J. Cleland, A new approach to modelling the effective thermal conductivity of heterogeneous materials, Int. J. Heat Mass Transfer 49 (2006) 3075–3083.
[36] S. Lapointe, K. Zhang, M. McNenly, Reduced chemical model for low and high-temperature oxidation of fuel blends relevant to internal combustion engines, Proc. Combust. Inst. 37 (2019) 789–796.
[37] Q. Lin, K.L. Tay, D. Zhou, W. Yang, Development of a compact and robust Polyoxymethylene Dimethyl Ether 3 reaction mechanism for internal combustion engines, Energy Convers Manag. 185 (2019) 35–43.
[38] S. Vasu, D. Davidson, Z. Hong, V. Vasudevan, R. Hanson, N-dodecane oxidation at high-pressures: Measurements of ignition delay times and OH concentration time-histories, Proc. Combust. Inst. 32 (2009) 173–180.
[39] L. Cai, S. Jacobs, R. Langer, F. vom Lehn, K.A. Heufer, H. Pitsch, Auto-ignition of oxymethylene ethers (OMEn, n=2–4) as promising synthetic e-fuels from renewable electricity: shock tube experiments and automatic mechanism generation, Fuel 264 (2020) 116711.

[40] J. Van Oijen, L. De Goey, Modelling of premixed laminar flames using flamelet-generated manifolds, Combust. Sci. Technol. 161 (2000) 113–137.

[41] O. Gicquel, N. Darabiha, D. Thévenin, Liminar premixed hydrogen/air counterflow flame simulations using flame prolongation of ILDM with differential diffusion, Proc. Combust. Inst. 28 (2000) 1901–1908.

[42] H. Bao, H.Y. Akargun, D. Roekaerts, B. Somers, The inclusion of scalar dissipation rate in modeling of an n-dodecane spray flame using flamelet generated manifold, Combust. Flame 249 (2023) 112610.

[43] R. Bilger, S.S. arner, R. Kee, On reduced mechanisms for methane-air combustion in nonpremixed flames, Combust. Flame 80 (1990) 135–149.

[44] H. Pitsch, N. Peters, A consistent flamelet formulation for non-premixed combustion considering differential diffusion effects, Combust. Flame 114 (1998) 26–40.

[45] M. Ihme, L. Shunn, J. Zhang, Regularization of reaction progress variable for application to flamelet-based combustion models, J. Comput. Phys. 231 (2012) 7715–7721.

[46] P. Rahnama, A. Maghbouli, H. Bao, A. Vasavan, R. Novella, B. Somers, Generalizing progress variable definition in CFD simulation of combustion systems using tabulated chemistry models, Appl. Energy Combust. Sci. 14 (2023) 100132.

[47] J. Matheis, H. Müller, C. Lenz, M. Pfitzner, S. Hickel, Volume translation methods for real-gas computational fluid dynamics simulations, J. Supercrit Fluid 107 (2016) 422–432.

[48] U. Egüz, S. Ayyapureddi, C. Bekdemir, B. Somers, P. de Goey, Manifold resolution study of the FGM method for an igniting diesel spray, Fuel 113 (2013) 228–238.

[49] J. Verner, Some Runge–Kutta formula pairs, SIAM J. Numer. Anal. 28 (1991) 496–511.

[50] S. Gottlieb, C.-W. Shu, E. Tadmor, Strong stability-preserving high-order time discretization methods, SIAM Rev. 43 (2001) 89–112.

[51] T. Xuan, H. Li, Y. Wang, Y. Chang, M. Jia, Z. He, Q. Wang, J. Cao, R. Payri, A conceptual model of polyoxymethylene dimethyl ether 3 (PODE3) spray combustion under compression ignition engine-like conditions, Combust. Flame 261 (2024) 113296.

[52] A. Saghafian, V. Terrapon, H. Pitsch, An efficient flamelet-based combustion model for compressible flows, Combust. Flame 162 (2015) 652–667.

[53] G. van den Oord, V. Azizi, M. Fathi, S. Hickel, Dynamic multi-level load balancing for scalable simulations of reacting multiphase flows, Int. J. High Perform. Comput. Appl. 39 (2025) 519–531, http://dx.doi.org/10.1177/10943420251329199.